LETTER

A map of the large day–night temperature gradient of a super-Earth exoplanet

Brice-Olivier Demory[1], Michael Gillon[2], Julien de Wit[3], Nikku Madhusudhan[4], Emeline Bolmont[5], Kevin Heng[6], Tiffany Kataria[7], Nikole Lewis[8], Renyu Hu[9,10], Jessica Krick[11], Vlada Stamenković[9,10], Björn Benneke[10], Stephen Kane[12] & Didier Queloz[1]

Over the past decade, observations of giant exoplanets (Jupiter-size) have provided key insights into their atmospheres[1,2], but the properties of lower-mass exoplanets (sub-Neptune) remain largely unconstrained because of the challenges of observing small planets. Numerous efforts to observe the spectra of super-Earths—exoplanets with masses of one to ten times that of Earth—have so far revealed only featureless spectra[3]. Here we report a longitudinal thermal brightness map of the nearby transiting super-Earth 55 Cancri e (refs 4, 5) revealing highly asymmetric dayside thermal emission and a strong day–night temperature contrast. Dedicated space-based monitoring of the planet in the infrared revealed a modulation of the thermal flux as 55 Cancri e revolves around its star in a tidally locked configuration. These observations reveal a hot spot that is located 41 ± 12 degrees east of the substellar point (the point at which incident light from the star is perpendicular to the surface of the planet). From the orbital phase curve, we also constrain the nightside brightness temperature of the planet to $1,380 \pm 400$ kelvin and the temperature of the warmest hemisphere (centred on the hot spot) to be about 1,300 kelvin hotter ($2,700 \pm 270$ kelvin) at a wavelength of 4.5 micrometres, which indicates inefficient heat redistribution from the dayside to the nightside. Our observations are consistent with either an optically thick atmosphere with heat recirculation confined to the planetary dayside, or a planet devoid of atmosphere with low-viscosity magma flows at the surface[6].

We observed the super-Earth 55 Cancri e for 75 h in total from 15 June to 15 July 2013 in the 4.5-μm channel of the Spitzer Space Telescope Infrared Array Camera (IRAC). The observations were split into eight continuous visits, each spanning 9 h and corresponding to half of the 18-h orbital period of 55 Cancri e. We acquired a total of 4,981,760 frames in subarray mode with an individual 0.02-s integration time. We extract the photometric time series from the raw frames using a previously described[4] aperture photometry pipeline. Each of the eight resulting light curves exhibit periodic flux variations due to the strong intra-pixel sensitivity of the IRAC detector combined to Spitzer's pointing wobble. The data reduction of this data set has been published elsewhere[7], but a summary is provided in Methods.

We analyse the light curves using a Markov chain Monte Carlo (MCMC) algorithm[8]. We simultaneously fit the eight half phase curves and a model of the detector systematics. Our MCMC algorithm includes an implementation of a pixel-level correction[9] and propagates the contribution from correlated noise in the data to the system best-fit parameters. In our implementation of the method, we build a sub-pixel mesh of n^2 grid points, evenly distributed along the x and y axes. Similar to a previous study[10], we find that the full-width at half-maximum (FWHM) of the point response function (PRF) along the x and y axes

of the detector evolves with time and allows further improvement to the systematics correction. We thus combine the pixel-mapping algorithm with a linear function of the FWHM of the PRF along each axis. We find that this model provides the best correction to the data. The free planetary parameters in the MCMC fit are the phase-curve amplitude and offset (the angle between the peak of the modulation and the substellar point), the occultation depth, the impact parameter, the orbital period, the transit centre and the transit depth. The functional form of the phase curve used in this fit is detailed in Methods. We combine the data points into 30-s bins for computing efficiency, which has previously been shown to have no effect on the derived parameters[7,11]. We find an average photometric precision of 363 p.p.m. per 30 s, and evaluate the level of correlated noise in the data for each data set using a time-averaging technique[12]. Results from the MCMC fits are shown in Table 1. We perform two additional analyses of this data set (see Methods) using a different model for the pixel-level correction, which results in phase-curve parameters in agreement with our main analysis.

Table 1 | 55 Cancri e planetary parameters

Basic planetary parameters	
Planet-to-star radius ratio, $R_p/R_\star$	$0.0187^{+0.0007}_{-0.0007}$
$b = a\cos(i)/R_\star$ ($R_\star$)	$0.41^{+0.05}_{-0.05}$
$T_0 - 2{,}450{,}000$ (BJD$_{TDB}$)	$5733.013^{+0.007}_{-0.007}$
Orbital period, P (days)	$0.736539^{+0.000007}_{-0.000007}$
Orbital semi-major axis, a (AU)	$0.01544^{+0.00009}_{-0.00009}$
Orbital inclination, i (°)	$83.3^{+0.9}_{-0.8}$
Mass*, M_p ($M_\oplus$)	$8.08^{+0.31}_{-0.31}$
Radius, R_p ($R_\oplus$)	$1.91^{+0.08}_{-0.08}$
Mean density, ρ_p (g cm^{-3})	$6.4^{+0.8}_{-0.7}$
Surface gravity, $\log[g_p$ (cm s^{-2})]	$3.33^{+0.04}_{-0.04}$
Planetary emission parameters from this work	
Phase-curve amplitude, A_{phase} (p.p.m.)	197 ± 34
Phase-curve offset, θ_{phase} (degrees east)	41 ± 12
Mid-eclipse occultation depth (p.p.m.)	154 ± 23
Maximum hemisphere-averaged temperature (K)	$2{,}697^{+268}_{-275}$
Minimum hemisphere-averaged temperature (K)	$1{,}376^{+344}_{-451}$
Average dayside temperature (K)	$2{,}349^{+188}_{-193}$

Results are from the MCMC combined fit. Values indicated are the median of the posterior distributions and the 1σ credible intervals. $R_\star$, stellar radius; b, impact parameter; T_0, transit centre; BJD, barycentric Julian date; TDB, barycentric dynamical time; $M_\oplus$, Earth mass; $R_\oplus$, Earth radius. *Mass prior distribution obtained from ref. 30.

[1]Astrophysics Group, Cavendish Laboratory, JJ Thomson Avenue, Cambridge CB3 0HE, UK. [2]Institut d'Astrophysique et de Géophysique, Université de Liège, allée du 6 Aout 17, 4000 Liège, Belgium. [3]Department of Earth, Atmospheric and Planetary Sciences, Massachusetts Institute of Technology, 77 Massachusetts Avenue, Cambridge, Massachusetts 02139, USA. [4]Institute of Astronomy, University of Cambridge, Cambridge CB3 0HA, UK. [5]NaXys, Department of Mathematics, University of Namur, 8 Rempart de la Vierge, 5000 Namur, Belgium. [6]University of Bern, Center for Space and Habitability, Sidlerstrasse 5, CH-3012, Bern, Switzerland. [7]Astrophysics Group, School of Physics, University of Exeter, Stocker Road, Exeter EX4 4QL, UK. [8]Space Telescope Science Institute, Baltimore, Maryland 21218, USA. [9]Jet Propulsion Laboratory, California Institute of Technology, Pasadena, California 91109, USA. [10]Division of Geological and Planetary Sciences, California Institute of Technology, Pasadena, California 91125, USA. [11]Spitzer Science Center, MS 220-6, California Institute of Technology, Jet Propulsion Laboratory, Pasadena, California 91125, USA. [12]Department of Physics and Astronomy, San Francisco State University, 1600 Holloway Avenue, San Francisco, California 94132, USA.
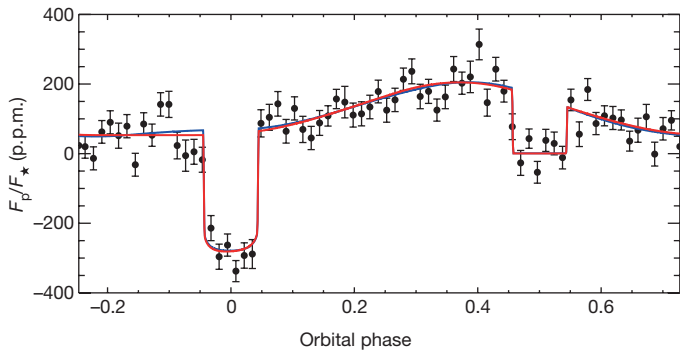
Figure 1 | 55 Cancri e Spitzer/IRAC 4.5-μm phase curve. Photometry for all eight data sets combined and folded onto the 0.74-day orbital period of 55 Cancri e. The black filled circles represent the relative flux ($F_p/F_\star$) variation in phase and are data binned per 15 min. The best-fit model using a three-longitudinal-band model is shown in red; the best-fit model using a one-longitudinal-band model is shown in blue. The error bars are the standard deviation of the mean within each orbital-phase bin.

The combined light curve (Fig. 1) exhibits a flux increase that starts slightly before the transit and reaches a maximum at 2.1 ± 0.6 h before opposition. We find a phase-curve peak amplitude of 197 ± 34 p.p.m., a minimum of 48 ± 34 p.p.m. and an occultation depth of 154 ± 23 p.p.m. (mid-eclipse).

We find that stellar variability could not cause the observed phase variation. The host is known to be an old, quiet star with a rotation period of 42 days that shows, on rare occasions, variability at the 6-millimagnitude level, corresponding to <1% coverage in star spots[13]. The periodic modulation that we observe is equal to the planetary orbital period and has a shape that remains consistent over the 4 weeks of the Spitzer observations. At infrared wavelengths, the effect of starspots on the photometry is markedly reduced[14], but it is still possible that 1% spot coverage could produce a signal of the order of 200 p.p.m. However, the periodicity of the signal produced by such a starspot would be similar to the stellar rotation.

We also investigate the amplitude of the ellipsoidal effects[15] caused by 55 Cancri e on its host star and find an expected amplitude of 0.6 p.p.m. The reciprocal effect from the host star on the planet would translate to an effect of about 1 p.p.m. (ref. 16). None of these features would be detectable in our data set. In addition, ellipsoidal variations have a frequency that is twice that of the orbital period of the planet. For these two reasons, we discard the possibility that ellipsoidal variations are at the origin of the observed signal.

An alternative way to mimic the orbital phase curve would be a scenario in which 55 Cancri e induces starspots on the stellar surface

via magnetic field interactions, which would produce a photometric modulation that is synchronized with the orbital period of the planet[17]. It has been suggested that the amplitude of these interactions increases with the ratio of the planetary mass to its orbital semi-major axis[17]; however, currently, there is no robust evidence for star–planet interactions even for planets with masses of 3–5 that of Jupiter on 0.9–5-day orbital periods. 55 Cancri e is an exoplanet with a mass of 0.02 Jupiter masses in a 0.74-day orbit; considering the large body of work on star–planet interactions[18], we deem it unlikely that 55 Cancri e could induce synchronized starspot patterns on its host star. Therefore, we assume in the following that the observed modulation originates from the planet itself.

The shape of the phase curve of 55 Cancri e provides constraints on the thermal brightness map of the planet. The phase-curve amplitude translates to a warmest-hemisphere-averaged brightness temperature of $2,697^{+268}_{-275}$ K at 4.5 μm, and a coolest-hemisphere-averaged brightness temperature of $1,376^{+344}_{-451}$ K. We find that the hot spot is centred on the meridian located $41° \pm 12°$ east of the substellar point. We longitudinally map the dayside of 55 Cancri e using an MCMC implementation[19]. This method was developed to map exoplanets and to mitigate the degeneracy between the planetary brightness distribution and the system parameters. We model the planetary dayside using two different prescriptions, similar to a previous study[20]. In the first model, we use a single longitudinal band (Fig. 2, left) with a position and width that are adjusted in the MCMC fit. The second model is similar to the 'beach-ball model'[21] that uses three longitudinal bands with fixed positions and widths (Fig. 2, right). In both cases, the relative brightness between each longitudinal band is adjusted in the MCMC fit.

The large day–night temperature difference of more than 1,300 K indicates a lack of strong atmospheric circulation redistributing energy from the dayside to the nightside of the planet. Such a large contrast could potentially be explained by the extremely high stellar irradiation received on the dayside, owing to which the radiative timescale might be shorter than the advective timescale, as has been suggested for highly irradiated hot Jupiters, which have H_2-dominated atmospheres[22]. However, the mass, radius and temperature of the planet are inconsistent with the presence of an H_2-dominated atmosphere[7,23], which is supported by the non-detection of H absorption in the Lyman-α[24] region of the spectrum, although an atmosphere with a higher mean molecular weight cannot be ruled out. It is possible that a high-mean-molecular-weight atmosphere of 55 Cancri e, for example, consisting largely of H_2O or CO_2, could also have a lower radiative timescale compared to the advective timescale, thereby explaining the inefficient circulation. However, the observed brightness temperature is unexpectedly high for such an explanation, because H_2O and CO_2 both have substantial opacity in the IRAC 4.5-μm bandpass, owing to which the upper, cooler regions of the atmosphere are probed preferentially.
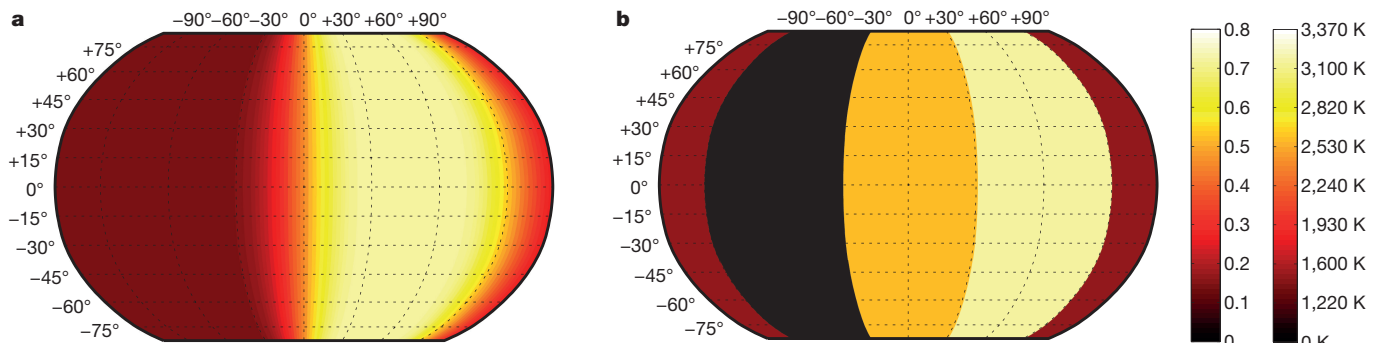

Figure 2 | Longitudinal brightness maps of 55 Cancri e. Longitudinal brightness distributions as retrieved from the Spitzer/IRAC 4.5-μm phase curve. The planetary dayside is modelled using two prescriptions. **a**, One-longitudinal-band model, with the band position, width and brightness adjusted in the fit. **b**, Three-longitudinal-band model, with the band positions and widths fixed, but their relative brightnesses adjustable. The colour scales indicate the planetary brightness normalized to the stellar-average brightness and the brightness temperature for each longitudinal band.

The maximum hemisphere-averaged temperature of $2{,}700 \pm 270$ K is marginally greater than the highest permissible equilibrium temperature, which is possible for the planetary surface, but implausible higher up in the atmosphere unless the atmosphere is host to strong thermal inversion[25]. Alternatively, the data may be explained by a planet devoid of a thick atmosphere of any composition that also has a low albedo. Such a hypothesis could explain both the radius of the planet, which is consistent with a purely rocky composition, as well as the lack of strong atmospheric circulation.

The substantial day–night temperature contrast observed is seemingly incongruous with the observation of a large offset of the hot spot $41°$ east from the substellar point. Such a shift of the hot spot requires efficient energy circulation in the atmosphere[22], contrary to the large day–night contrast observed. An alternative explanation is that the planet harbours an optically thick atmosphere in which heat recirculation takes place, but only on the dayside, while the gases condense out on the planetary nightside[26], possibly forming clouds[20]. However, such a scenario requires either the atmosphere to be dominated by vapours of high-temperature refractory compounds, for example, silicates[27,28], or the nightside temperatures to be below freezing so that volatiles such as H_2O condense; the latter is ruled out by our observed nightside temperature of $1{,}380 \pm 400$ K. It is possible that there are strong longitudinal inhomogeneities in the chemical composition and emissivity in the atmosphere causing a longitudinally varying optical depth in the 4.5-μm bandpass that could potentially explain the data. Alternatively, the hot-spot offset may be driven by an eastward molten lava flow on the dayside surface of the planet, which would have a viscosity more similar to water at room temperature than to solid rock. At the observed maximum hemisphere-averaged temperature of about $2{,}700$ K, silicate-based rocks are expected to be molten[29], whereas the nightside temperature of about $1{,}380$ K can be cool enough to sustain a partially to mostly solid surface, where rock viscosities would be several orders of magnitude larger than on the dayside.

Additional constraints resulting from the estimated atmospheric escape induced by the nearby host star suggest that it is unlikely that 55 Cancri e is harbouring a thick atmosphere. We find that the surface pressure of 55 Cancri e needs to be larger than 31 kbar for the planet to survive over the lifetime of its star, which supports a scenario in which 55 Cancri e has no atmosphere (see Methods).

From the fit from the three-longitudinal-band model, we find that the region of maximum thermal emission is located $30°$–$60°$ east of the substellar point, with brightness temperatures in excess of $3{,}100$ K. We find that tidal dissipation can explain only a fraction of this re-emitted radiation (see Methods), suggesting that an additional, currently unknown source provides a sizeable contribution to the infrared emission of 55 Cancri e.

Online Content Methods, along with any additional Extended Data display items and Source Data, are available in the online version of the paper; references unique to these sections appear only in the online paper.

1. Burrows, A. S. Highlights in the study of exoplanet atmospheres. *Nature* **513**, 345–352 (2014).
2. Heng, K. & Showman, A. P. Atmospheric dynamics of hot exoplanets. *Annu. Rev. Earth Planet. Sci.* **43**, 509–540 (2015).
3. Knutson, H. A. et al. *Hubble Space Telescope* near-IR transmission spectroscopy of the super-Earth HD 97658b. *Astrophys. J.* **794**, 155 (2014).
4. Demory, B.-O. et al. Detection of a transit of the super-Earth 55 Cancri e with warm *Spitzer*. *Astron. Astrophys.* **533**, A114 (2011).
5. Winn, J. N. et al. A super-Earth transiting a naked-eye star. *Astrophys. J.* **737**, L18 (2011).
6. Solomatov, V. in *Treatise on Geophysics* Vol. 9 (ed. Schubert, G.) 91–119 (Elsevier, 2007).
7. Demory, B.-O., Gillon, M., Madhusudhan, N. & Queloz, D. Variability in the super-Earth 55 Cnc e. *Mon. Not. R. Astron. Soc.* **455**, 2018–2027 (2016).
8. Gillon, M. et al. The TRAPPIST survey of southern transiting planets. I. Thirty eclipses of the ultra-short period planet WASP-43 b. *Astron. Astrophys.* **542**, A4 (2012).
9. Stevenson, K. B. et al. Transit and eclipse analyses of the exoplanet HD 149026b using BLISS mapping. *Astrophys. J.* **754**, 136 (2012).
10. Lanotte, A. A. et al. A global analysis of *Spitzer* and new HARPS data confirms the loneliness and metal-richness of GJ 436 b. *Astron. Astrophys.* **572**, A73 (2014).
11. Deming, D. et al. *Spitzer* secondary eclipses of the dense, modestly-irradiated, giant exoplanet HAT-P-20b using pixel-level decorrelation. *Astrophys. J.* **805**, 132 (2015).
12. Pont, F., Zucker, S. & Queloz, D. The effect of red noise on planetary transit detection. *Mon. Not. R. Astron. Soc.* **373**, 231–242 (2006).
13. Fischer, D. A. et al. Five planets orbiting 55 Cancri. *Astrophys. J.* **675**, 790–801 (2008).
14. Berta, Z. K. et al. The GJ1214 super-Earth system: stellar variability, new transits, and a search for additional planets. *Astrophys. J.* **736**, 12 (2011).
15. Mazeh, T. & Faigler, S. Detection of the ellipsoidal and the relativistic beaming effects in the CoRoT-3 lightcurve. *Astron. Astrophys.* **521**, L59 (2010).
16. Budaj, J. The reflection effect in interacting binaries or in planet–star systems. *Astron. J.* **141**, 59 (2011).
17. Shkolnik, E., Bohlender, D. A., Walker, G. A. H. & Collier Cameron, A. The on/off nature of star–planet interactions. *Astrophys. J.* **676**, 628–638 (2008).
18. Miller, B. P., Gallo, E., Wright, J. T. & Pearson, E. G. A comprehensive statistical assessment of star–planet interaction. *Astrophys. J.* **799**, 163 (2015).
19. de Wit, J., Gillon, M., Demory, B.-O. & Seager, S. Towards consistent mapping of distant worlds: secondary-eclipse scanning of the exoplanet HD 189733b. *Astron. Astrophys.* **548**, A128 (2012).
20. Demory, B.-O. et al. Inference of inhomogeneous clouds in an exoplanet atmosphere. *Astrophys. J.* **776**, L25 (2013).
21. Cowan, N. B. et al. Alien maps of an ocean-bearing world. *Astrophys. J.* **700**, 915–923 (2009).
22. Showman, A. P., Fortney, J. J., Lewis, N. K. & Shabram, M. Doppler signatures of the atmospheric circulation on hot Jupiters. *Astrophys. J.* **762**, 24 (2013).
23. Gillon, M. et al. Improved precision on the radius of the nearby super-Earth 55 Cnc e. *Astron. Astrophys.* **539**, A28 (2012).
24. Ehrenreich, D. et al. Hint of a transiting extended atmosphere on 55 Cancri b. *Astron. Astrophys.* **547**, A18 (2012).
25. Madhusudhan, N. & Seager, S. On the inference of thermal inversions in hot Jupiter atmospheres. *Astrophys. J.* **725**, 261–274 (2010).
26. Heng, K. & Kopparla, P. On the stability of super-Earth atmospheres. *Astrophys. J.* **754**, 60 (2012).
27. Schaefer, L. & Fegley, B. Jr. Atmospheric chemistry of Venus-like exoplanets. *Astrophys. J.* **729**, 6 (2011).
28. Miguel, Y., Kaltenegger, L., Fegley, B. & Schaefer, L. Compositions of hot super-Earth atmospheres: exploring *Kepler* candidates. *Astrophys. J.* **742**, L19 (2011).
29. Lutgens, F. K. & Tarbuck, E. J. *Essentials of Geology* 7th edn, Ch. 3 (Prentice Hall, 2000).
30. Nelson, B. E. et al. The 55 Cancri planetary system: fully self-consistent N-body constraints and a dynamical analysis. *Mon. Not. R. Astron. Soc.* **441**, 442–451 (2014).

Author Contributions B.-O.D. initiated and led the Spitzer observing programme, conducted the data analysis and wrote the paper. M.G. performed an independent analysis of the dataset. E.B. carried out the simulations assessing the amplitude of tidal heating in the interior of 55 Cancri e. J.d.W. performed the longitudinal mapping of the planet. N.M. wrote the interpretation section with inputs from E.B., K.H., V.S., R.H., N.L. and T.K. J.K., B.B., S.K. and D.Q. contributed to the observing programme. All authors commented on the manuscript.

Author Information Reprints and permissions information is available at www.nature.com/reprints. The authors declare no competing financial interests. Readers are welcome to comment on the online version of the paper. Correspondence and requests for materials should be addressed to B.-O.D. (bod21@cam.ac.uk).

METHODS

Data reduction. We observed four phase curves of 55 Cancri e with the Spitzer Space Telescope in the IRAC/4.5-μm channel as part of our program ID 90208. Because of downlink constraints, these four phase-curve observations were split into eight separate observations (or Astronomical Observation Requests, AORs) each lasting half an orbit of 55 Cancri e. Details of each AOR are provided in Extended Data Table 1. The corresponding data can be accessed from the Spitzer Heritage Archive (http://sha.ipac.caltech.edu). All AORs were acquired in stare mode using a constant exposure time (0.02 s). All our data were obtained using the Pointing Calibration and Reference Sensor (PCRS) peak-up mode, which allows the observer to place the target on a precise location on the detector to mitigate the intra-pixel sensitivity variations. This observing mode increases the pointing stability and reduces the level of correlated noise in the data by a factor of 2–3 (ref. 31). AOR 48072960 experienced a 30-min interruption during data acquisition, which forces us to treat both parts of that AOR separately in the rest of this section. We do not retain the 30-min-long PCRS sequences in our analysis because the motion of the star on the detector yields large correlated noise in these data sets. Our reduction uses the basic calibrated data (BCD) that are downloaded from the Spitzer Archive. The BCD are Flexible Image Transfer System (FITS) data cubes consisting of 64 frames of 32 × 32 pixels each. Our data reduction code reads each frame, converts fluxes from the Spitzer units of specific intensity (MJy sr^{-1}) to photon counts, and transforms the data time-stamps from BJD$_{UTC}$ to BJD$_{TDB}$ using existing procedures[32]. We did not deem it necessary to discard specific sub-array frames. During the reduction process, we compute the flux, position and FWHM in each of the 64 frames of each data cube; the frames for which any of these parameters differ from the median by more than 5σ are discarded. The centroid position on the detector is determined by fitting a Gaussian to the marginal x, y distributions using the *GCNTRD* procedure of the IDL Astronomy User's Library[33]. We also fit a two-dimensional Gaussian to the stellar PRF following previous studies[34]. We find that determining the centroid position using *GCNTRD* results in a smaller dispersion of the fitted residuals by 10% to 15% across our data set, in agreement with other Spitzer analyses[35]. We then perform aperture photometry for each data set using a modified version of the *APER* procedure using aperture sizes of ranging from 2.2 to 4.4 pixels in 0.2-pixel intervals. We choose the optimal aperture size on the basis of minimizing r.m.s. × β_{red}^2 for each AOR, where r.m.s. is the root-mean-square of the photometric time series and β_{red} is the red-noise contribution[8]. The red noise is assessed over 60-min timescales because shorter timescales are irrelevant for the phase-curve signal whose periodicity is 18 h. We measure the background contribution on each frame using an annulus located 10 to 14 pixels from the centroid position. Our code also determines the FWHM of the PRF along the x and y axes. We use a moving average based on forty consecutive frames to discard data points that differ from the median by more than 5σ in background, (x, y) position or FWHM. We find that, on average, 0.06% of the data points are discarded. The resulting time series are combined into 30-s bins to speed up the analysis; this binning has been shown to have no influence on the values or uncertainties of the system parameters[7]. We show the optimal aperture size, corresponding r.m.s. and β_{red} for each data set in Extended Data Table 1.

Photometric analysis. *Intra-pixel sensitivity correction*. We use an implementation of the BLISS (BiLinearly-Interpolated Sub-pixel Sensitivity)[9] to account for the intra-pixel sensitivity variations, as was similarly used in a previous study using the same data set[7].

The BLISS algorithm uses a bilinear interpolation of the measured fluxes to build a pixel-sensitivity map. The data are thus self-calibrated. Our implementation of this algorithm is included in the Markov chain Monte Carlo (MCMC) framework presented in ref. 8. The improvement introduced by a pixel-mapping technique such as BLISS requires that the stellar centroid remains in a relatively confined area on the detector, which warrants an efficient sampling of the x–y region and, hence, an accurate pixel map. In our implementation of the method, we build a sub-pixel mesh of n^2 grid points, evenly distributed along the x and y axes. The BLISS algorithm is applied at each step of the MCMC fit. The number of grid points is determined at the beginning of the MCMC by ensuring that at least five valid photometric measurements are located in each mesh box. Similar to two recent studies[7,10], we find that a further reduction of the level of correlated noise in the photometry is achieved by the inclusion of the FWHM of the PRF along the x and y axes as extra parameters in the baseline model. The PRF evolves with time and its properties are not accounted for by the BLISS algorithm. We thus combine the BLISS algorithm with a linear function of the FWHM of the PRF along the x and y axes. In addition, the baseline model for each AOR includes a flux constant.

We find that including a model of the FWHM of the PRF decreases the Bayesian Information Criterion (BIC)[36] by $\Delta BIC = 591$. We show the raw data sets with the best-fit instrumental + astrophysical model superimposed in red in Extended Data Figs 1–3. The corrected photometry is shown in Extended Data Figs 4–6. The phase-curve modulation is clearly noticeable in each AOR. The behaviour of the photometric r.m.s. as a function of binning is shown for each data set in Extended Data Fig. 7.

Model comparison. In our first MCMC analysis, to model the variation in the infrared emission of the planet we use $F = F_p + Tr + Oc$ (in which F is the observed flux, F_p is the phase modulation driven by the planet, Tr is the transit model and Oc is the occultation model), and a Lambertian[37] functional form for F_p

$$F_p = A_{phase} \frac{\sin(z) + (\pi - z)\cos(z)}{\pi}$$

in which A_{phase} is the phase amplitude and

$$\cos(z) = -\sin(i)\cos[2\pi(\phi + \theta_{phase})]$$

$$\phi = \frac{2\pi}{P}(t - T_0)$$

where θ_{phase} is the phase-curve offset, ϕ is the phase angle, i is the orbital inclination of the planet, P the orbital period, T_0 the transit centre and t is time.

The transit- (Tr) and occultation- (Oc) light-curve model MA (ref. 38) are summarized as

$$Tr = MA(d_{Ftr}, P, b, M_\star, c_1, c_2, t)$$

$$Oc = MA(d_{Foc}, P, b, M_\star, t)$$

in which $d_{F_{tr}}$ and $d_{F_{oc}}$ are the transit and occultation depths, respectively, b is the impact parameter, $M_\star$ is the stellar mass, and $c_1 = 2u_1 + u_2$ and $c_2 = u_1 - 2u_2$ are the limb-darkening linear combinations, with u_1 and u_2 the quadratic coefficients obtained from theoretical tables[39] using published stellar parameters[40].

We also experimented using a sinusoid for the phase variation: $F_p = A_{phase}\cos(\phi + \theta_{phase})$. The fit using a sinusoid results in an amplitude $A_{phase} = 218 \pm 50$ p.p.m. and an offset value $\theta_{phase} = 68° \pm 24°$ east of the substellar point, in agreement with our results using a Lambertian functional form ($A_{phase} = 197 \pm 34$ p.p.m. and $\theta_{phase} = 41° \pm 12°$).

The Lambertian sphere model provides a better fit to the data than does the sinusoid model, with $\Delta BIC = 11$.

We also perform another MCMC analysis with no phase-curve model, hence removing two degrees of freedom (phase amplitude and phase offset). We find $\Delta BIC = 21$ in favour of the model including the phase-curve model.

We also run an MCMC fit that includes the phase amplitude, but not the phase offset. We find that this fit produces only a marginal χ^2 improvement over the MCMC fit with the no-phase-curve model, but this improvement is penalized by the extra degree of freedom according to the BIC. We indeed obtain a $\Delta BIC = 25$ in favour of the model including the phase-curve offset.

Altogether, this model comparison confirms that a phase-curve model that includes a phase offset is the favoured functional form according to the BIC.

Additional analyses. We conduct two additional analyses of our entire data set to assess the robustness of our initial detection that used the BLISS mapping technique. In these two analyses, we use different approaches to (1) model the intra-pixel sensitivity of the detector and (2) change the input data format.

In the first analysis, we use a simple polynomial detrending approach with a functional form that includes only the centroid position (fourth-order) and FWHM (first-order). We experimented with different polynomial orders (from one to four) for these two parameters and found that this combination globally minimizes the BIC. Each AOR has its own set of baseline coefficients. As for the BLISS mapping, the polynomial detrending is included in the MCMC fit so the baseline model and the system parameters are adjusted simultaneously to efficiently propagate the uncertainties to the final parameters. We find a level of correlated noise in the data that is only slightly larger (about 10%) than that obtained with the BLISS mapping technique. Using this method we find a phase-curve minimum of 36 ± 41 p.p.m., a maximum of 187 ± 41 p.p.m. and an offset of $50° \pm 13°$ east of the substellar point; using the BLISS mapping, the corresponding values are 47 ± 34 p.p.m., 197 ± 34 p.p.m. and $41° \pm 12°$ east. As previously shown[10], the addition of the FWHM of the PRF in the baseline model substantially improves a fit based on only a centroid position, and, most importantly, it enables an acceptable fit to 8-h time series.

In the second analysis, we aim to assess whether the phase-curve signal persists when we split our input data. All our AORs have durations of nearly 9 h, and we elect to split each of them in two to reduce the duration of each individual data set to 4.5 h. The functional forms of the baseline models are the same as for the analysis using the unsegmented input data, described above. In this additional test, we find a phase-curve minimum of 51 ± 51 p.p.m., a maximum of 216 ± 51 p.p.m. and an offset of $54° \pm 16°$ east of the substellar point. These results are in good

agreement with our main analysis. The uncertainties in the phase-curve parameters are larger in this case because of the time-series segmentation, which does not constrain the baseline coefficients as effectively as for longer data sets. The phase curves obtained from these additional analyses are shown in Extended Data Fig. 8.

We finally note that the phase-curve peak is located close to the start of half of our observations and towards the end of the other half data sets, which was necessary owing to Spitzer downlink limitations. We deem this pattern purely coincidental for two reasons. First, if our reported phase curve was due to uncorrected systematics, then it would be unlikely that the systematics would produce an upward trend in half of the data and a downward trend in the other half. These data sets are independent and there is no relationship between those obtained from transit to occultation and those obtained from occultation to transit. There is also no correlation with the centroid position on the detector. Second, if the phase-peak offset occurred after or before this discontinuity, then it would have been clearly detected in the continuous parts of our data set; however, only gradual slopes are seen in both data sets. A comparison with data obtained in the same year with the Microvariability and Oscillations of STars (MOST) satellite (D. Dragomir, personal communication) shows an agreement in the phase-curve amplitude and offset values derived from both facilities.

Longitudinal mapping. The key features of the phase curve of 55 Cancri e translate directly into constraints on maps[41,42] assuming a tidally locked planet on a circular orbit. A planetary phase curve $F_p/F_\star$ ($F_\star$ is the flux from the star) measures the planetary hemisphere-averaged relative brightness $\langle I_p \rangle / \langle I_\star \rangle$ as

$$\frac{F_p}{F_\star}(\alpha) = \frac{\langle I_p \rangle(\alpha)}{\langle I_\star \rangle}\left(\frac{R_p}{R_\star}\right)^2$$

in which α is the orbital phase, R_p is the planetary radius and $R_\star$ is the stellar radius.

The longitudinal mapping technique used here[19] aims to mitigate the degeneracy between the distribution of the planetary thermal brightness and the system parameters. This part of the analysis is independent of the light-curve analysis presented above. Therefore, here we fix the system parameters to those derived from a previous study[7], which is based on the entire 55 Cancri e Spitzer data set. Using this prior information for the purpose of longitudinal mapping is adequate because the degeneracy between the planetary brightness distribution and the system parameters is only relevant in the context of eclipse mapping[19]. We follow the same approach as for Kepler-7b (ref. 20) and use two families of models, similar to the 'beach-ball models' introduced in ref. 21: one using n longitudinal bands with fixed positions on the dayside, and another using longitudinal bands whose positions and widths are jump parameters in the MCMC fit. We choose a three-fixed-band model and one-free-band model to extract both the longitudinal dependence of the dayside brightness of 55 Cancri e and the extent of its 'bright' area. Increasing n to five yields a larger BIC than for $n = 3$. For both models, we compute the amplitude of each band from their simulated light curve using a perturbed singular-value decomposition method. The one-free-band model (Fig. 2, left) yields a uniformly bright longitudinal area extending from $5° \pm 18°$ west to $85° \pm 18°$ east with a relative brightness of 0.72 ± 0.18, compared to a brightness of 0.15 ± 0.05 for the rest of the planet. The three-fixed-band model yields bands of relative brightness decreasing from the west to the east: <0.21 (3σ upper limit), 0.58 ± 0.15 and 0.74 ± 0.15, compared to the nightside contribution of 0.17 ± 0.06.

Variability of the thermal emission of 55 Cancri e. Variability in the thermal emission of 55 Cancri e between 2012 and 2013, has previously been determined from occultation measurements[7]. Several tests regarding the robustness of the variability pattern were conducted, including three different analyses that used BLISS mapping, polynomial detrending and a pixel-level decorrelation method[11]. These three approaches confirmed the variability of the thermal emission of the planet between 2012 and 2013 with similar uncertainties. Therefore, we consider it very likely that the emission of the planet is varying, but on timescales that are substantially longer than the timescale of the 2013 observations alone (a month) used here. No variability is reported in the 2013 data alone[7]. These factors justify our combining of the 2013 observations and our use of a single phase-curve model. Furthermore, we detect the phase-curve shape in all individual data sets in addition to the combined phase-folded time series. This strengthens our conclusion that it is unlikely that stellar variability would cause the combined phase-curve shape from individual stellar events taken at different times over the month of observations.

Brightness temperatures. We use an observed infrared spectrum of 55 Cancri e (ref. 43) to compute the brightness temperatures in the IRAC 4.5-μm bandpass from the $F_p/F_\star$ values derived from the MCMC fits.

Constraints on the atmosphere of 55 Cancri e. If an atmosphere was present, then the large temperature contrast between the dayside and nightside hemispheres suggests that the radiative cooling time (t_{rad}) is less than the dynamical time scale (t_{dyn}), resulting in a poor redistribution of heat from the dayside to the nightside. This sets a constraint on the mean molecular weight, which we may estimate. The zonal velocity is $v \approx \sqrt{\mathcal{R}\Delta T} \approx 1 \text{ km s}^{-1}$, in which $\mathcal{R}$ is the specific gas constant, $\Delta T = 1,460 \text{ K}$ is the temperature difference between the hemispheres and we have

ignored an order-unity correction factor associated with the pressure difference between the hemispheres[44]. If we enforce $t_{rad} < t_{dyn}$, then for the mean molecular weight μ we obtain

$$\mu > \frac{\mathcal{R}_{univ}(\Delta T)^{1/3}}{T_{day}^2}\left(\frac{P_{day}}{\sigma_{SB}R_p\kappa g}\right)^{2/3}$$

in which $\mathcal{R}_{univ} = 8.3144598 \times 10^7 \text{ erg K}^{-1} \text{ g}^{-1}$ is the universal gas constant, $T_{day} = 2,700 \text{ K}$ is the dayside temperature, σ_{SB} is the Stefan–Boltzmann constant, $R_p = 1.91R_\oplus$ is the planetary radius ($R_\oplus$ is the Earth radius), $\kappa = 2/7$ is the adiabatic coefficient, $g = 10^{3.33} \text{ cm s}^{-2}$ is the surface gravity and P_{day} is the dayside pressure—the only unknown parameter in this expression. If we set $P_{day} = 1$ bar, then $\mu > 9$. This estimate further suggests that a hydrogen-dominated atmosphere is unlikely, and sets a lower limit on the mean molecular weight.

It is unlikely that 55 Cancri e is harbouring a thick atmosphere, owing to its proximity to its star. If we assume energy-limited escape[45], then the atmosphere needs to have sufficient mass to survive for the stellar age, which translates into a lower limit on the required surface pressure

$$P > \frac{\mathcal{L}_X R_p t_\star g}{16\pi G M_p a^2}$$

in which $\mathcal{L}_X$ is the X-ray luminosity of the star, $t_\star$ is the stellar age, G is Newton's gravitational constant, $M_p = 8.08M_\oplus$ is the planetary mass ($M_\oplus$ is the Earth mass) and $a = 0.01544$ au is the orbital semi-major axis. If $\mathcal{L}_X = 4 \times 10^{26} \text{ erg s}^{-1}$ (ref. 24) and $t_\star = 8$ Gyr, then $P > 31$ kbar; in other words, the surface pressure of 55 Cancri e needs to be larger than 31 kbar to survive atmospheric escape over the stellar lifetime. Despite the uncertainties associated with estimating the mass loss due to atmospheric escape, this estimate is conservative because the star probably emitted higher X-ray luminosities in the past. Our suggestion of an atmosphereless 55 Cancri e is consistent with the trends predicted for super-Earths[45].

Hence, it is unlikely that the large infrared peak offset is due to an atmosphere rich with volatiles. It is more likely that the infrared phase curve of 55 Cancri e is probing non-uniformities associated with its molten rocky surface.

Tidal heating. Because 55 Cancri is a multi-planet system, the eccentricity and obliquity of 55 Cancri e are excited, owing to the presence of the outer planets. This creates a tidal heat flux that is responsible, in part, for the thermal emission of the planet. To evaluate the contribution of the tidal heat flux to the measured thermal emission, we investigate the possible values of the eccentricity and obliquity of 55 Cancri e for different tidal dissipation using N-body simulations (using Mercury-T; ref. 46). We use the orbital elements and masses for the four outer planets[30] and the most recent values[7] for the mass, radius and orbital semi-major axis of 55 Cancri e.

We find that the obliquity of 55 Cancri e is very low ($<1°$) and that the eccentricity is about 10^{-3} for the eight orders of magnitude (10^{-5}–10 times the dissipation of Earth $\sigma_\oplus$) we consider for the tidal dissipation of 55 Cancri e. The corresponding tidal heat flux ϕ_{tides} or tidal temperature ($\phi_{tides}/\sigma)^{1/4}$ increase with the dissipation in 55 Cancri e, from 10^{-3} W m^{-2} (a few kelvin) to 10^6 W m^{-2} (about 2,000 K). We calculate the occultation depth at 4.5-μm for a range of eccentricities and albedos (0.0–1.0) to enable a comparison with the output of the dynamical simulations (Extended Data Fig. 9). We find that a combination of large dissipation ($10\sigma_\oplus$), eccentricity and obliquity can explain the level of thermal emission observed in 2013; however, these solutions do not allow us to reproduce the nightside temperature. In our configuration (no heat re-distribution and assuming an isotropic tidal heat flux), tides do not match our measurements, so an additional heat source is probably responsible for at least part of the large planetary thermal emission observed in 2013.

Code availability. The code used to perform the aperture photometry on the Spitzer data sets presented here is publicly available from the IDL Astronomy User's Library at http://idlastro.gsfc.nasa.gov. We have opted not to make the MCMC code available, but the corrected photometry for each data set is available online as Source Data.

31. Ballard, S. *et al.* Kepler-93b: a terrestrial world measured to within 120 km, and a test case for a new *Spitzer* observing mode. *Astrophys. J.* **790,** 12 (2014).
32. Eastman, J., Siverd, R. & Gaudi, B. S. Achieving better than 1 minute accuracy in the heliocentric and barycentric Julian Dates. *Publ. Astron. Soc. Pacif.* **122,** 935–946 (2010).
33. Landsman, W. B. The IDL Astronomy User's Library. In *Astronomical Data Analysis Software and Systems II* Vol. 52 of *ASP Conf. Ser.* (eds Hanisch, R. J. *et al.*) 246–248 (Astronomical Society of the Pacific, 1993).
34. Agol, E. *et al.* The climate of HD 189733b from fourteen transits and eclipses measured by *Spitzer*. *Astrophys. J.* **721,** 1861–1877 (2010).
35. Beerer, I. M. *et al.* Secondary eclipse photometry of wasp-4b with warm spitzer. *Astrophys. J.* **727,** 23 (2011)
36. Schwarz, G. Estimating the dimension of a model. *Ann. Stat.* **6,** 461–464 (1978).

37. Sobolev, V. V. *Light Scattering in Planetary Atmospheres* Vol. 76 of *International Series of Monographs in Natural Philosophy* Ch. 9 (Pergamon Press, 1975) [transl.].
38. Mandel, K. & Agol, E. Analytic light curves for planetary transit searches. *Astrophys. J.* **580,** L171–L175 (2002).
39. Claret, A. & Bloemen, S. Gravity and limb-darkening coefficients for the *Kepler*, CoRoT, *Spitzer, uvby, UBVRIJHK*, and Sloan photometric systems. *Astron. Astrophys.* **529,** A75 (2011).
40. von Braun, K. *et al.* 55 Cancri: stellar astrophysical parameters, a planet in the habitable zone, and implications for the radius of a transiting super-Earth. *Astrophys. J.* **740,** 49 (2011).
41. Knutson, H. A. *et al.* A map of the day–night contrast of the extrasolar planet HD 189733b. *Nature* **447,** 183–186 (2007).
42. Cowan, N. B. & Agol, E. Inverting phase functions to map exoplanets. *Astrophys. J.* **678,** L129–L132 (2008).
43. Crossfield, I. J. M. ACME stellar spectra. I. Absolutely calibrated, mostly empirical flux densities of 55 Cancri and its transiting planet 55 Cancri e. *Astron. Astrophys.* **545,** A97 (2012).
44. Menou, K. Magnetic scaling laws for the atmospheres of hot giant exoplanets. *Astrophys. J.* **745,** 138 (2012).
45. Owen, J. E. & Wu, Y. Kepler planets: a tale of evaporation. *Astrophys. J.* **775,** 105 (2013).
46. Bolmont, E., Raymond, S. N., Leconte, J., Hersant, F. & Correia, A. C. M. *Mercury-T*: a new code to study tidally evolving multi-planet systems. Applications to Kepler-62. *Astron. Astrophys.* **583,** A116 (2015).
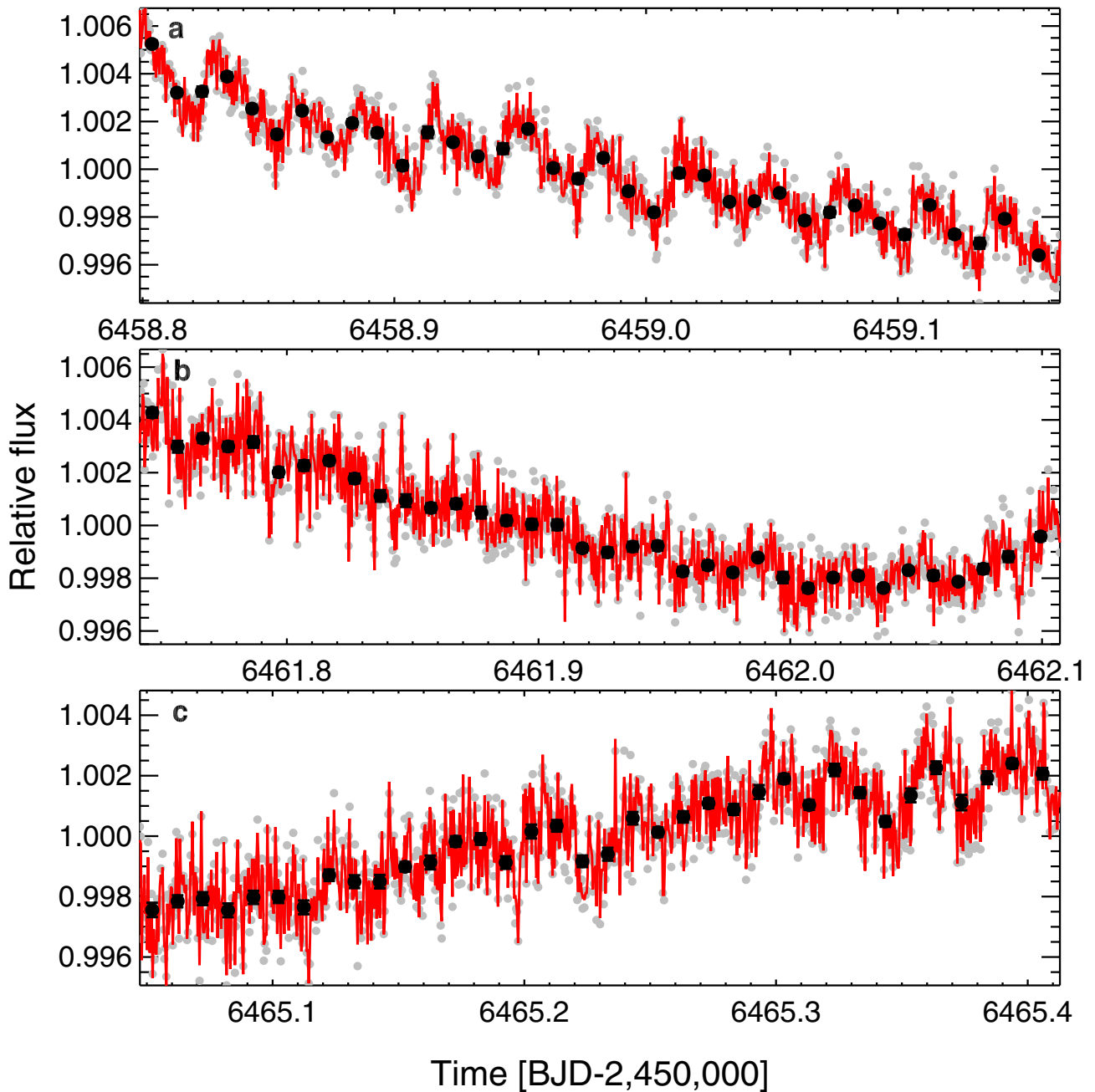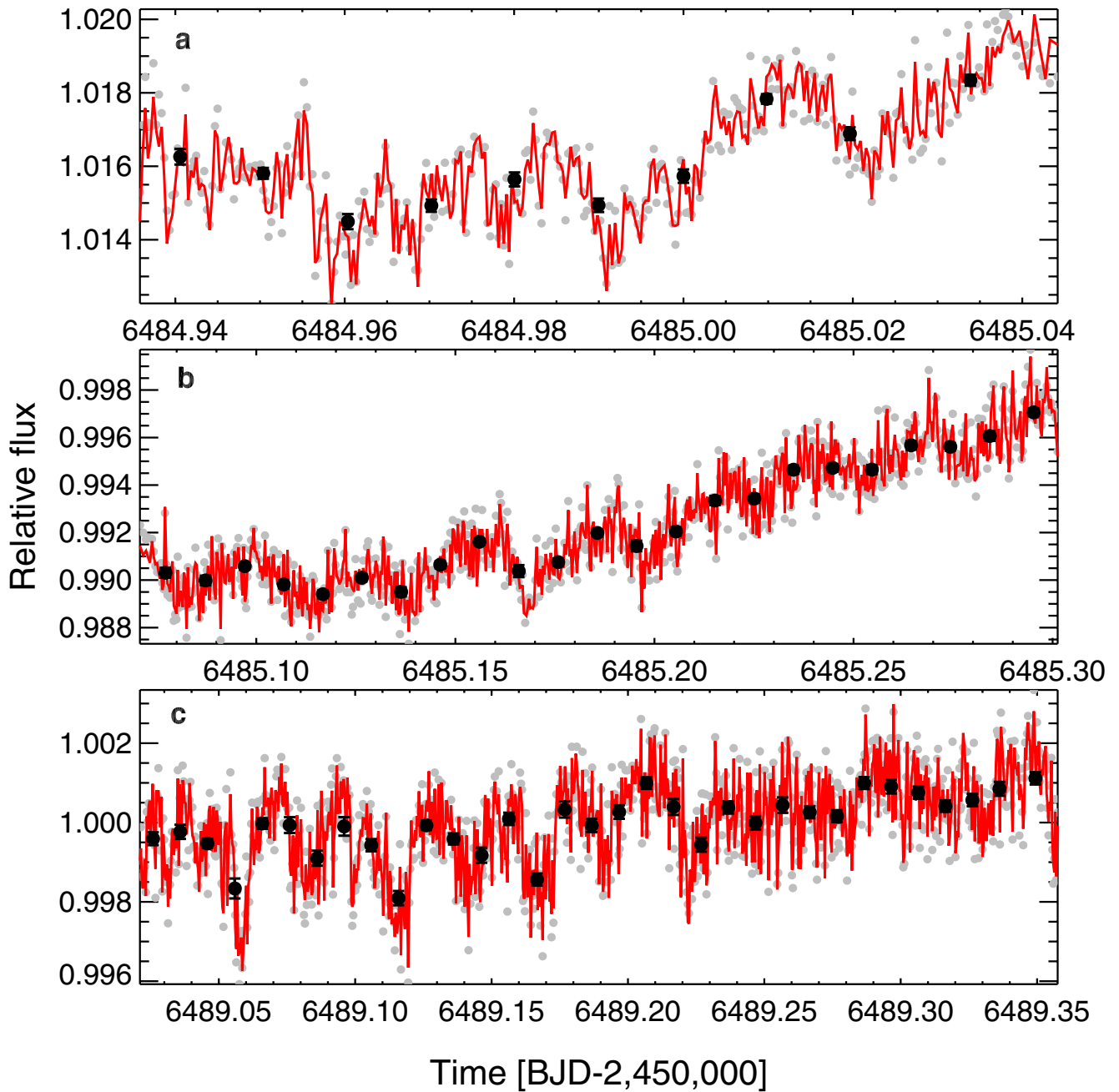
Extended Data Figure 1 | 55 Cancri e raw photometry. a–c, The raw data for time series acquired on 15 June 2013 (**a**), 18 June 2013 (**b**) and 21 June 2013 (**c**). The best-fi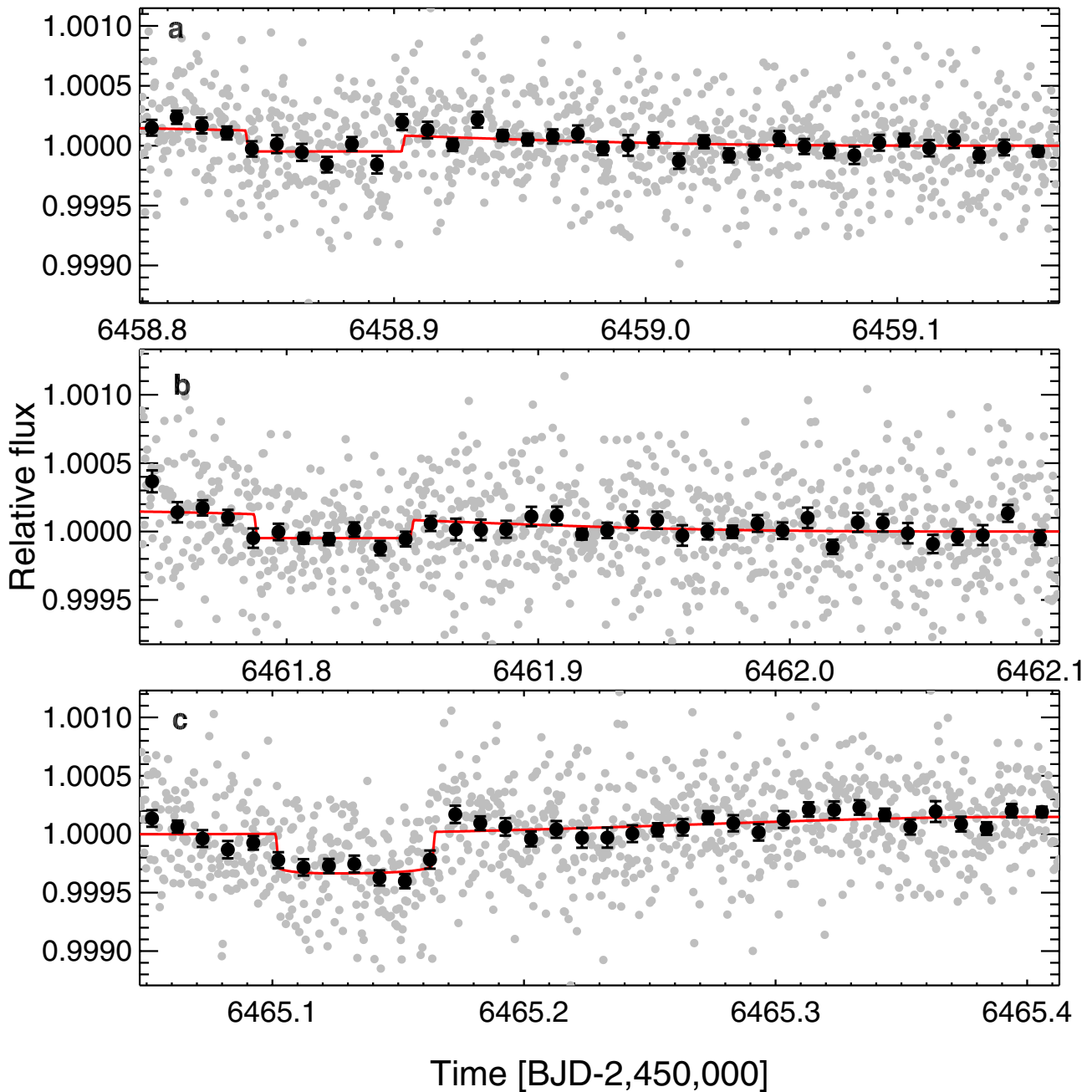t instrumental + astrophysical model is superimposed in red. Grey filled circles are data binned per 30 s. Black filled circles are data binned per 15 min. The error bars are the standard deviation of the mean within each time bin. BJD, barycentric Julian date.
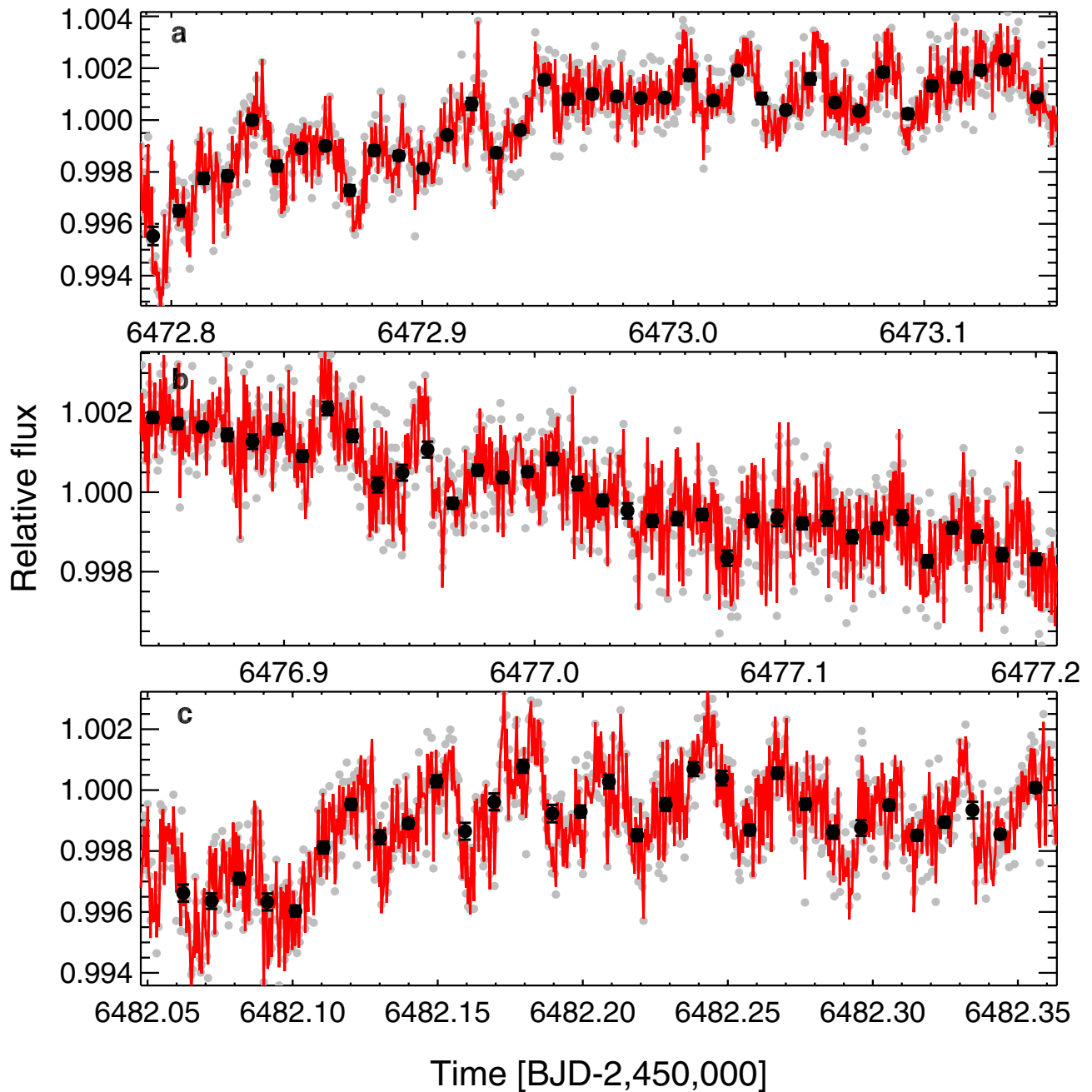
Extended Data Figure 2 | Continuation of Extended Data Fig. 1. a–c, The raw data for time series acquired on 29 June 2013 (**a**), 3 July 2013 (**b**) and 8 July 2013 (**c**).
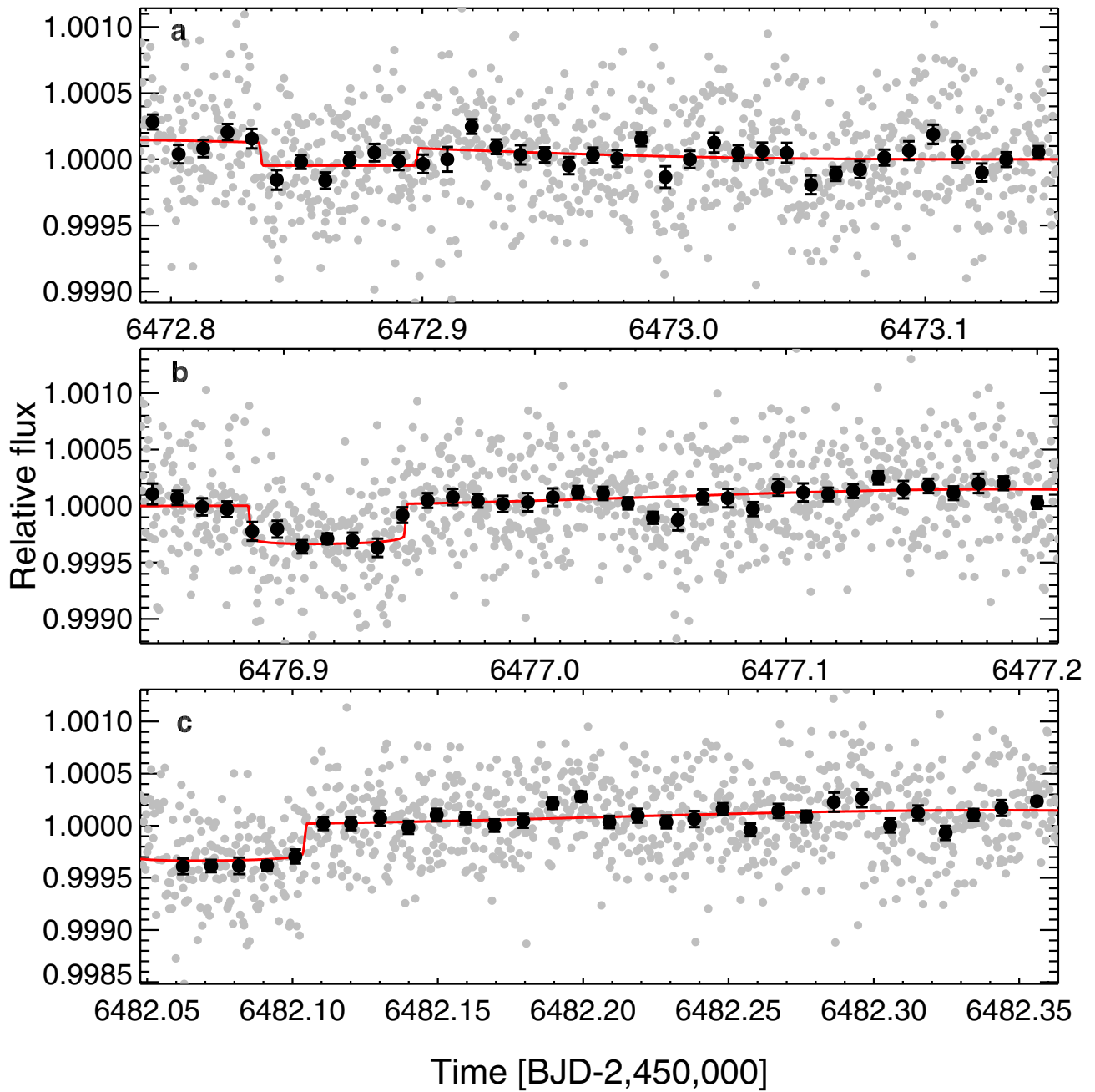
Extended Data Figure 3 | Continuation of Extended Data Fig. 1. a–c, The raw data for time series acquired on 11 July 2013 (**a**, **b**) and 15 July 2013 (**c**).

Extended Data Figure 4 | 55 Cancri e corrected photometry. a–c, The detrended data for time series acquired on 15 June 2013 (**a**), 18 June 2013 (**b**) and 21 June 2013 (**c**). The best-fit instrumental + astrophysical model is superimposed in red. Grey filled circles are data binned per 30 s. Black filled circles are data binned per 15 min. The error bars are the standard deviation of the mean within each time bin. BJD, barycentric Julian date.

Extended Data Figure 5 | Continuation of Extended Data Fig. 4. a–c, The detrended data for time-series acquired on 29 June 2013 (**a**), 3 July 2013 (**b**) and 8 July 2013 (**c**).
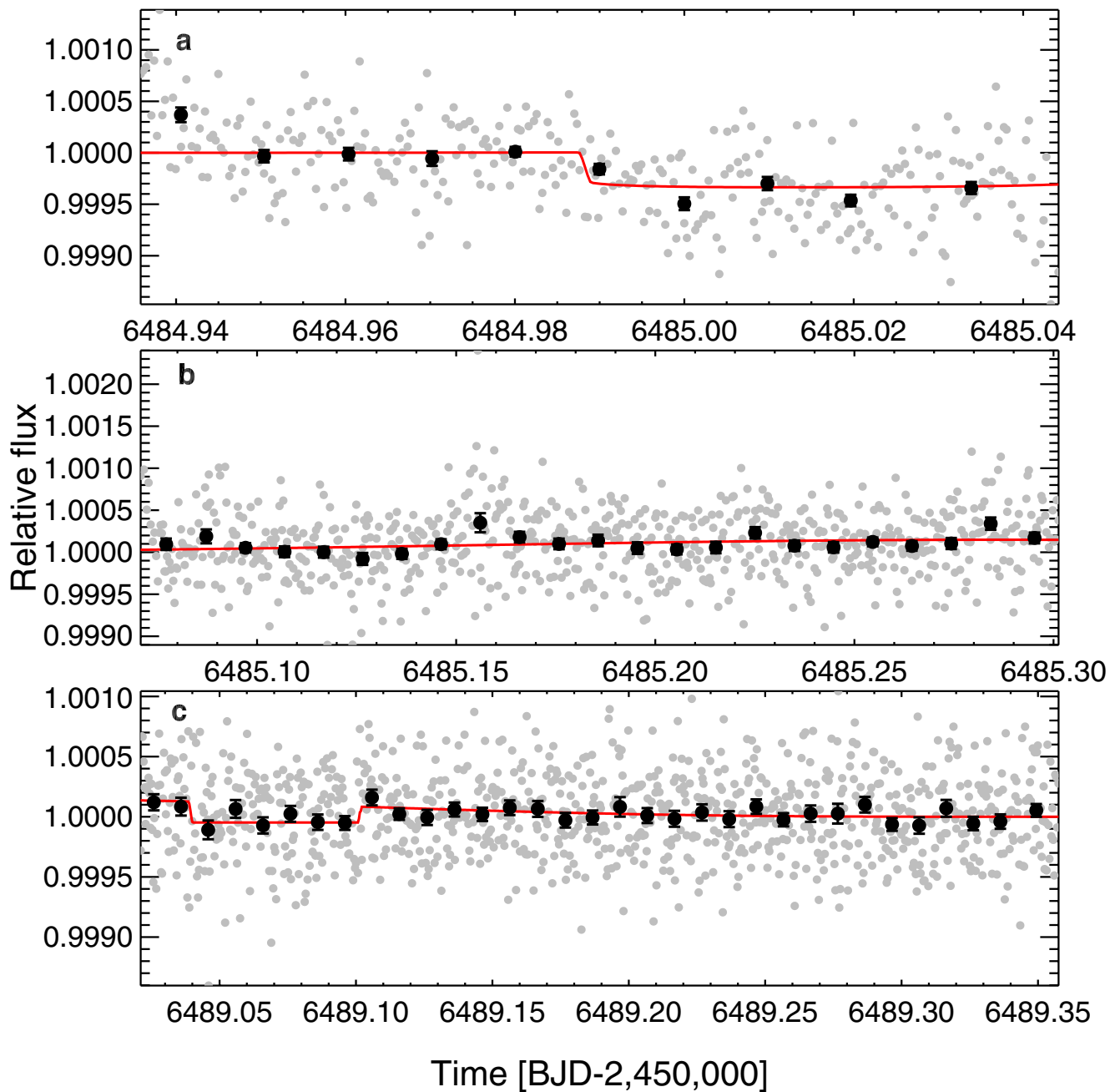
Extended Data Figure 6 | Continuation of Extended Data Fig. 4. a–c, The detrended data for time-series acquired on 11 July 2013 (**a**, **b**) and 15 July 2013 (**c**).
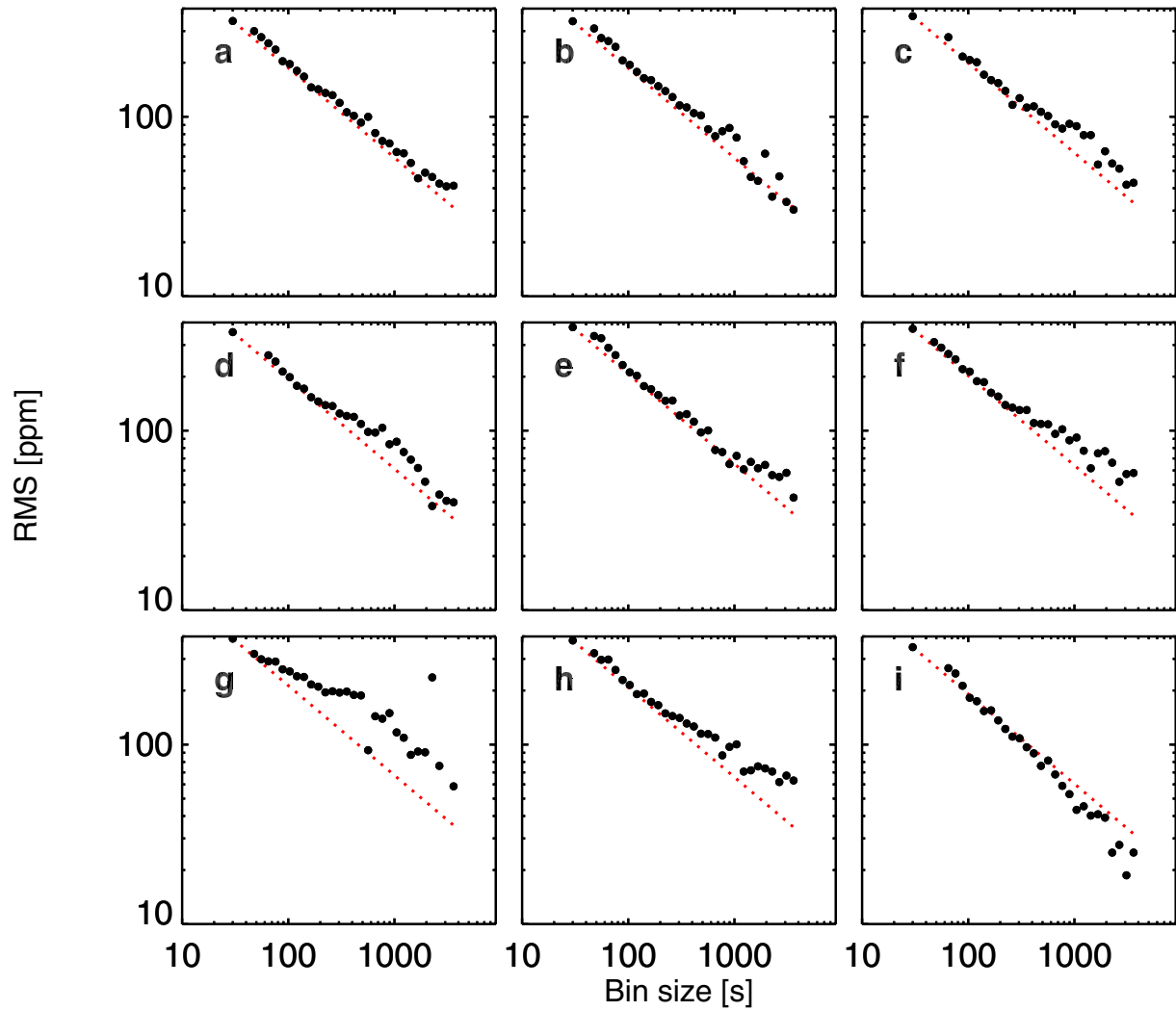
Extended Data Figure 7 | Photometric r.m.s. versus bin size for all data sets. a–i, Black filled circles indicate the photometric residual r.m.s. for different time bins. Each panel corresponds to each individual data set (**a–i**, increasing observing date). The expected decrease in Poisson noise normalized to an individual bin (30 s) precision is shown as a red dotted line.
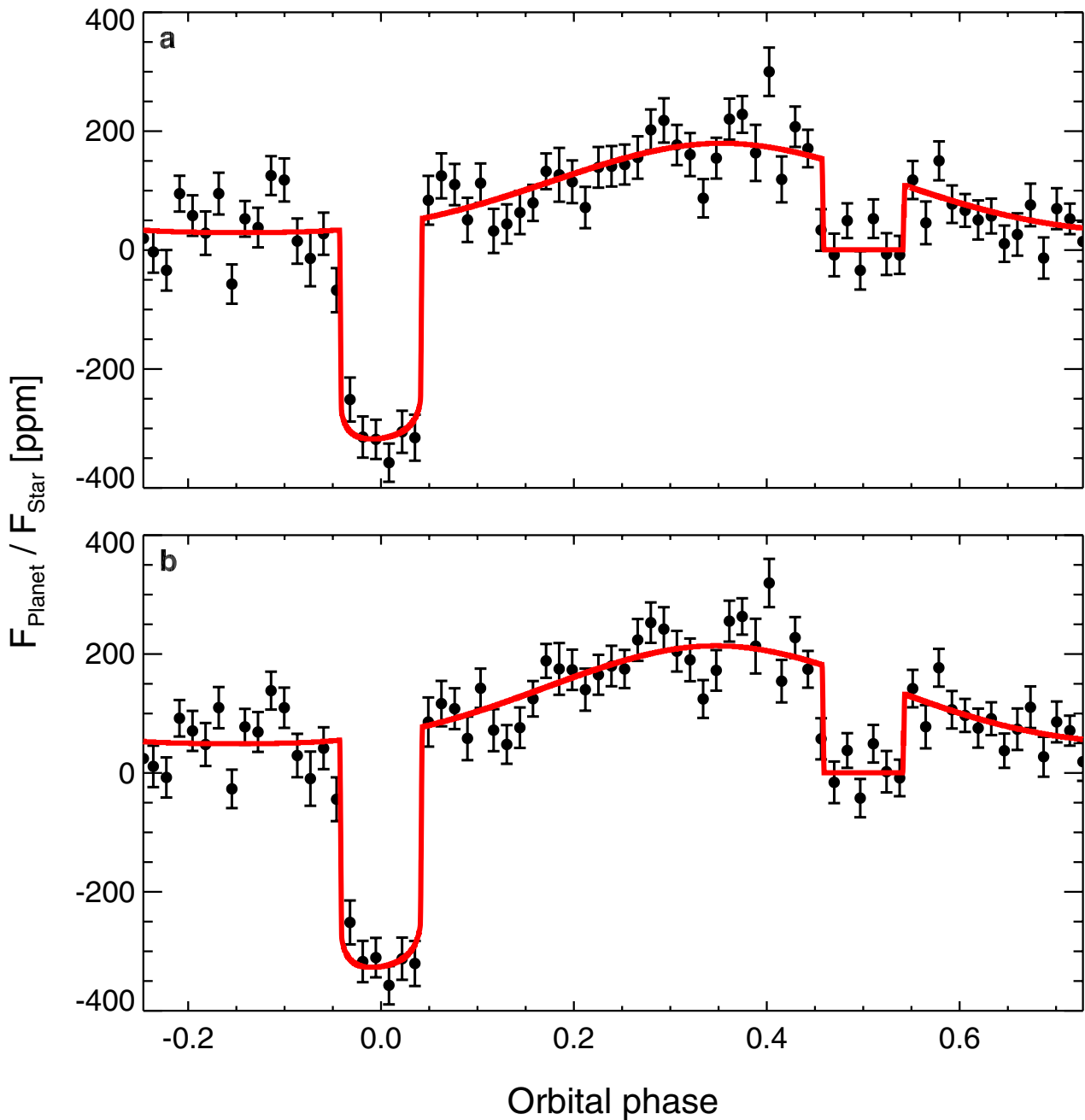
Extended Data Figure 8 | Polynomial-detrended phase-folded photometry. Photometry for all eight data sets combined and folded on the orbital period of 55 Cancri e. **a**, Fit results using the entire time series as input data. **b**, Fit results obtained by splitting the times series in two. Data in **a** and **b** represent the planet-to-star flux ratio (F_{planet}/F_{star}) variation in phase and are binned per 15 min; the error bars are the standard deviation of the mean within each orbital phase bin. The best-fit model is shown in red. Contrary to Fig. 1, these fits are obtained using polynomial functions of the centroid position and the FWHM of the PRF.
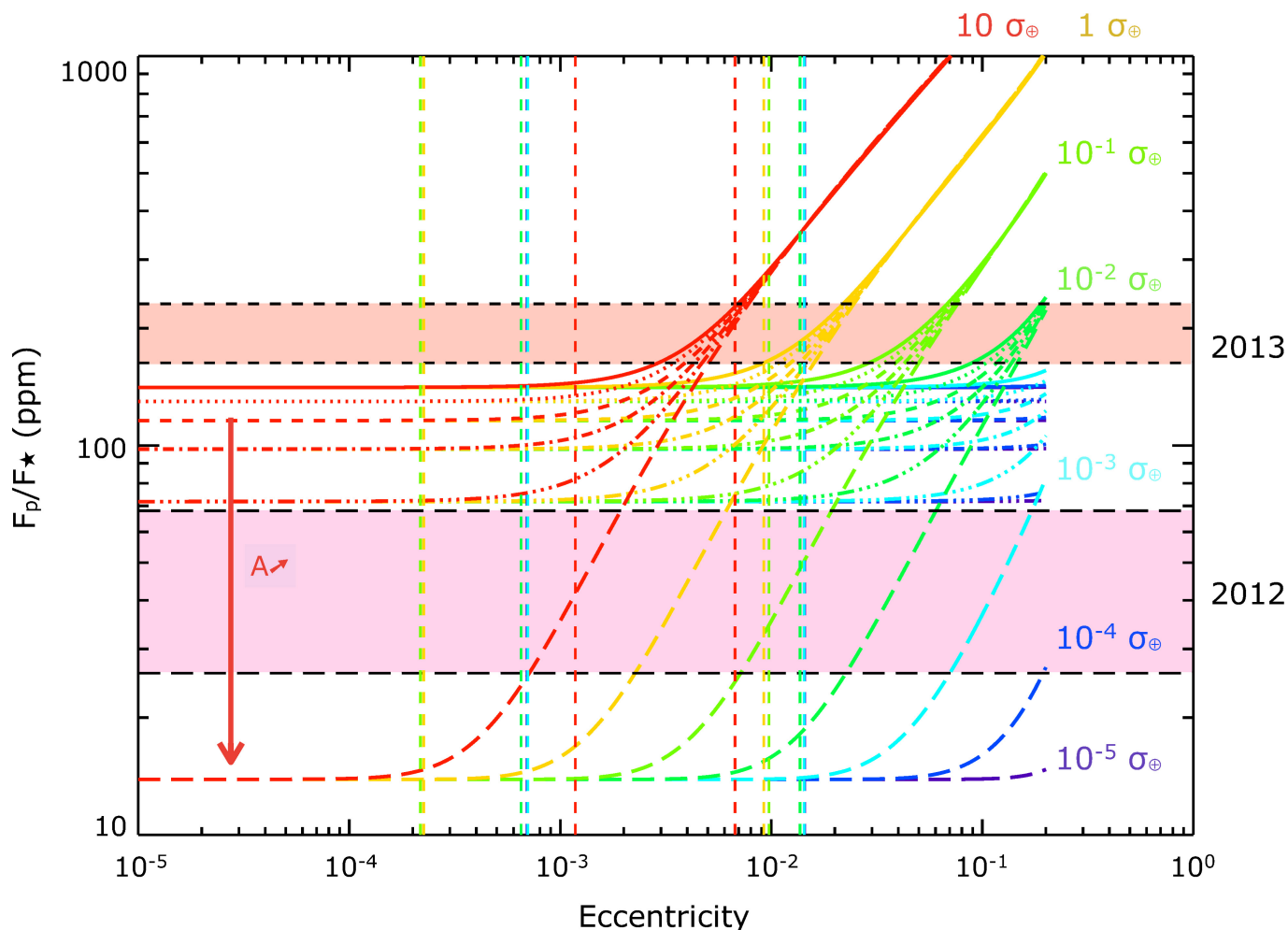
Extended Data Figure 9 | Tidal heating constraints for 55 Cancri e.
The planet-to-star flux ratio ($F_p/F_\star$) is shown as a function of the orbital eccentricity for different values of dissipation (relative to the Earth's $\sigma_\oplus$; indicated by the different colours) and albedos ('A', indicated by the different line styles, from 0.0 (solid) to 1.0 (long-dashed)). The pink and orange bands represent the occultation depth values measured in 2012 and 2013 with Spitzer, respectively. Vertical lines indicate the plausible range of the eccentricity of 55 Cancri e as determined from the N-body simulations for each dissipation value. The 2012 occultation depth can be matched for high albedos and a high dissipation, while the deeper 2013 occultation depth can be matched for the highest dissipation ($10\sigma_\oplus$) and the whole albedo range.

Extended Data Table 1 | 55 Cancri e Spitzer data set

Date [UT]	Program ID	AOR #	AOR duration [h]	Phase range	Aperture [pix]	Interp. n	RMS/30s [ppm]	β_r
2013-06-15	90208	48070144	8.8	0.40 - 0.89	2.6	64	341	1.17
2013-06-18	90208	48073216	8.8	0.39 - 0.89	3.0	64	340	1.00
2013-06-21	90208	48070656	8.8	0.88 - 0.38	2.8	70	363	1.00
2013-06-29	90208	48073472	8.8	0.39 - 0.89	3.0	58	354	1.16
2013-07-03	90208	48072448	8.8	0.90 - 0.39	3.2	69	376	1.34
2013-07-08	90208	48072704	8.0	0.94 - 0.39	2.6	77	370	1.03
2013-07-11	90208	48072960, p1	2.6	0.88 - 0.03	2.6	22	388	1.77
2013-07-11	90208	48072960, p2	5.5	0.07 - 0.38	2.6	58	389	1.83
2013-07-15	90208	48073728	8.1	0.43 - 0.89	3.4	73	348	1.00

Astronomical Observation Request (AOR) properties for the Spitzer/IRAC 4.5-μm data used here. This table also indicates the planetary orbital phase covered by each AOR as well as the number of interpolation points (n, 'Interp.') relevant to the BLISS algorithm. β_{red}, red-noise contribution to each AOR.